

# Model of a variable radio period for Saturn

B. Cecconi<sup>1</sup>

Department of Physics and Astronomy, University of Iowa, Iowa City, Iowa, USA

P. Zarka

Laboratoire d'Etudes Spatiales et d'Instrumentation en Astrophysique, Centre National de la Recherche Scientifique, Observatoire de Paris, Meudon, France

Received 16 February 2005; revised 21 July 2005; accepted 12 September 2005; published 3 December 2005.

[1] We propose an explanation for the variations at the 1% level of Saturn's radio rotation period measured at kilometer wavelengths. Because Saturn's kilometric radiation (SKR) is strongly controlled by the solar wind, we suggest that nonrandom variations of solar wind characteristics, especially its velocity, at Saturn may result in systematic displacement of the auroral sources in local time and finally in modifications of the apparent radio period. Alternatively, it may result in the superposition of two apparent periods, as also observed in Voyager data. We develop two simple models of local time variations of the SKR sources and analyze the conditions under which the measured radio period may be shifted by up to a few percent from the planet's sidereal period. Our results provide a possible explanation for the 1% variation observed and suggest that the dominant peak in the harmonic analysis of SKR variations seen by Voyager may be different from Saturn's sidereal rotation period. We relate the limitation in the accuracy of planetary rotation period determination to long-term variations of "control" parameters (like the solar wind velocity). One and a half to three years of continuous SKR observations with Cassini will be required to reliably and accurately derive Saturn's true sidereal period.

**Citation:** Cecconi, B., and P. Zarka (2005), Model of a variable radio period for Saturn, *J. Geophys. Res.*, 110, A12203, doi:10.1029/2005JA011085.

## 1. Introduction

[2] The sidereal rotation period of giant planets cannot be deduced from optical measurements because of the superimposed motion of the atmosphere. By contrast, high-latitude (auroral) radio emissions, which are attributed to electrons moving in the planet's magnetic field, are tied to the rotation of the planet's core. Variations of these auroral emissions were thus used to derive the true planetary rotation. In the case of Jupiter, *Higgins et al.* [1997] analyzed several 12-year and 24-year intervals of ground-based observations of the decameter radio emission and obtained an average sidereal period of 9 hours, 55 min, 29.68 s with individual determinations differing by no more than 0.08 s, i.e., a relative accuracy of the order of  $10^{-6}$ . Saturn's rotation period was derived from the analysis of 267 days of SKR (Saturn's auroral Kilometric Radiation) observations by Voyager 1 spacecraft and found to be  $P_V = 10$  hours, 39 min, 24 s  $\pm$  7 s (0.02% relative accuracy) [*Desch and Kaiser*, 1981].

[3] Analyzing further observations of SKR by the Ulysses spacecraft, *Galopeau and Lecacheux* [2000] (hereafter G00) found that Saturn's radio period is not constant. Spectral analysis of  $\sim 2$ -month intervals of Ulysses radio data recorded between late 1994 and early 1997 revealed fluctuations of the SKR period at the 1% level, the average period being 0.5% to 1% longer than  $P_V$ . Radio observations performed since early 2004 with the Radio and Plasma Wave Science experiment on board Cassini confirm the Ulysses results [*Gurnett et al.*, 2005].

[4] Note that in the Fourier spectrum of SKR time series (Figure 1 of *Desch and Kaiser* [1981]), a secondary peak is visible at  $\sim 10$  hours 41 min (i.e., 0.3% above  $P_V$ ), and there is also a small peak at  $\sim 10$  hours 45 min (1% longer than  $P_V$ , i.e., close to Ulysses and Cassini values).

[5] A change of the true sidereal period of Saturn ( $P_{\text{Sat}}$ ) is a priori excluded. The question is thus to explain the 1% variation of the SKR period and to estimate our ability to accurately determine  $P_{\text{Sat}}$  from radio measurements. If the observed variation is attributed to the SKR sources drifting around the planet, then, as a  $\sim 2$ -month interval corresponds to  $\sim 135$  rotations of Saturn, a variation of the radio period by 1% implies that the SKR sources must have made over one full turn around the magnetic pole during the time interval studied. This is incompatible with the fact that the SKR sources were found to be approximately fixed in local time (LT) and mostly located in the morning-to-noon sector

<sup>1</sup>Also at Laboratoire d'Etudes Spatiales et d'Instrumentation en Astrophysique, Centre National de la Recherche Scientifique, Observatoire de Paris, Meudon, France.

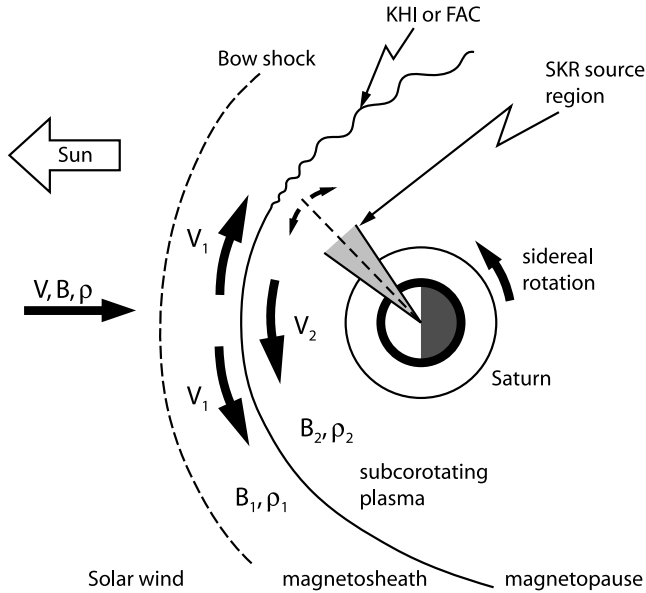


**Figure 1.** Sketch of the Saturn's kilometric radiation (SKR) source region as seen from the north magnetospheric pole (adapted from G00).  $V$ ,  $B$ , and  $\rho$  stand for the unperturbed solar wind velocity, magnetic field, and mass density.  $V_1$ ,  $B_1$ , and  $\rho_1$  represent the same quantities in the magnetosheath, which vary with the local time.  $V_2$ ,  $B_2$ , and  $\rho_2$  characterize the subcorotating kronian magnetoplasma. The main average SKR source location as derived by G95 is represented by the grey cone. Its LT position coincides with the locus of maximum algebraic difference between  $V_1$  and  $V_2$ , consistent with both the Kelvin-Helmholtz instability (KHI) (G95) and field-aligned currents (FAC) [Cowley *et al.*, 2004] theories. Solar wind variations imply variations of  $V_1$ ,  $B_1$ , and  $\rho_1$ , leading to back and forth motions of the SKR source versus LT, which are analyzed here.

of the auroral regions [Warwick *et al.*, 1981; Galopeau *et al.*, 1995], which is also the case for their UV auroral counterpart [Trauger *et al.*, 1998; Kurth *et al.*, 2005]. We propose below a model that reconciles the location of SKR sources in a restricted LT sector and the observed variations of the measured radio period.

## 2. SKR Source Location and Origin

[6] The SKR was discovered by the Voyager-PRA and -PWS experiments [Kaiser *et al.*, 1980; Warwick *et al.*, 1981; Gurnett *et al.*, 1981]. It is the most intense component of Saturn's low-frequency radio spectrum, covering the range between a few kHz and  $\sim 1.3$  MHz, with a maximum intensity between 100 and 400 kHz. Spectral structures such as arcs and bursts are visible in SKR dynamic spectra, although less organized than in the Jovian case (see reviews by Kurth and Zarka [2001] and Zarka and Kurth [2005]). Measured variations of the SKR polarization along the Voyager 1 and 2 flyby trajectories allowed Galopeau *et al.* [1995] (hereafter G95) to constrain the northern and southern SKR source locations. Conjugate high-latitude ( $\geq 80^\circ$ ) dayside sources fixed in LT were found, with a broad extent toward the morningside at lower latitudes (down to  $60^\circ$  at 0800–0900 LT) and a more limited one about 1900 LT.

Auroral UV emissions detected with HST (Hubble Space Telescope) are generally brighter in the morningside, consistent with the derived SKR source locations [Trauger *et al.*, 1998; Cowley *et al.*, 2004; Prangé *et al.*, 2004]. In spite of the fact that sources are approximately fixed in LT, SKR is strongly modulated at a period about 10 hours 39.4 min, interpreted as the sidereal planetary rotation period. The origin of the modulation is attributed to a magnetic anomaly at high latitudes [Galopeau *et al.*, 1991; Galopeau and Zarka, 1992; Ladreiter *et al.*, 1994], sweeping by a restricted LT region where electron precipitations are present.

[7] G95 proposed a Kelvin-Helmholtz instability (KHI) at the magnetopause as the source of accelerated electrons responsible for the auroral radio and UV emissions [Thompson, 1983]. As an alternative, Cowley *et al.* [2004] gave arguments in favor of upward field-aligned currents (FAC) at the morningside boundary between open and closed field lines as the primary source of Saturn's UV aurora and, as a consequence, of SKR. In both cases, the velocity shear between the partially corotating plasma inside the magnetopause and the shocked plasma flowing in the magnetosheath is believed to play a major role in the process leading to electron precipitation. The velocity of the plasma flowing in the magnetosheath depends on the solar wind velocity  $V$  and on the LT via the shape of the magnetopause (cf. G95, G00, and Figure 1). In addition, rotation-averaged SKR intensity variations appear strongly correlated to solar wind fluctuations, especially its ram pressure  $\rho V^2$  [Desch, 1982] and kinetic power flux  $\rho V^3$  [Desch and Rucker, 1983], with  $\rho$  the solar wind mass density and  $V$  its velocity. There is thus evidence that the solar wind velocity  $V$  plays a major role in SKR generation and especially in the LT location of its sources along the magnetopause.

## 3. Models of a Variable Radio Period

### 3.1. Solar Wind Influence on SKR Source Location

[8] According to G95 and G00, the dimensionless criterion defining a threshold for the KHI in the equatorial plane can be written

$$Q = \frac{|V_1 - V_2|^2}{\left(\frac{1}{\rho_1} + \frac{1}{\rho_2}\right) \frac{B_1^2}{\mu_0}}, \quad (1)$$

where  $V_1$  and  $V_2$  ( $\rho_1$  and  $\rho_2$ , respectively) are the flow velocities (the mass densities, respectively) on either side of the magnetopause, and  $B_1$  is the magnetic field in the magnetosheath (Figure 1).  $Q > 1$  corresponds to unstable domains along the magnetopause.  $V_1$  and  $\rho_1$  in the magnetosheath are related to the solar wind velocity  $V$  and density  $\rho$  via the model magnetopause described in G95 and G00.  $B_1$  is typically equal to  $\sim 7 \times B$ .

[9] Typical ranges of variation of  $B$ ,  $V$ , and  $\rho$  are displayed in Figure 2 for the year 1980, prior to the Voyager 1 Saturn encounter.  $B$  varies typically between 0.1 and 1–2 nT,  $V$  varies between about 300 and 600 km/s, and  $\rho$  varies between 0.5 and 5  $10^{-22}$  kg m $^{-3}$ . On the basis of these parameter ranges, Figure 3 illustrates the LT extent of the KHI domain along the equatorial magnetopause as a function of  $B$ ,  $V$ , or  $\rho$ , one parameter being variable and the two other ones kept constant in each plot. Following

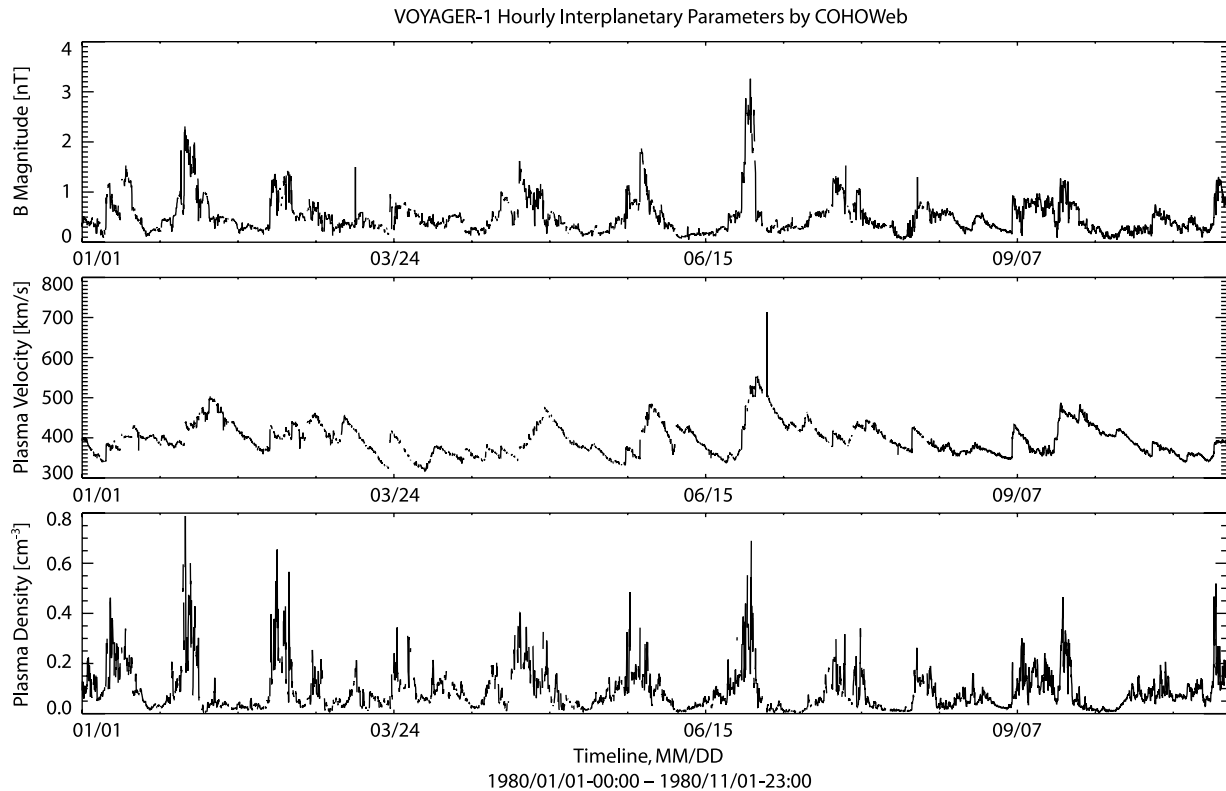


**Figure 2.** Solar wind magnetic field  $B$ , velocity  $V$ , and number density  $N$  variations measured by Voyager 1 from January to October 1980, prior to its closest approach to Saturn (1980/11/13). Mass density  $\rho$  is proportional to  $N$  ( $\rho \simeq 1.1 \times Nm_p$ ). Variations of  $V$  systematically follow a sawtooth shape, with steep increases and slow decreases.  $N$  is far more noisy, while  $B$  show a behavior intermediate of  $V$  and  $N$ . Data was provided by the NSSDC/COHWeb server.

G95 and G00, we take in the outer magnetosphere  $\rho_2 = 5.6 \cdot 10^{-22} \text{ kg m}^{-3}$  and a subcorotation velocity  $V_2 \sim 100 \text{ km/s}$  (with an azimuthal variation along the magnetopause). It appears from Figure 3 that, as expected from equation (1), the KHI domain expands with increasing  $V$  while  $B$  plays a stabilizing role. By contrast,  $\rho$  has a limited impact on the KHI domain over most of its range of variation. For typical solar wind parameters  $\rho = 10^{-22} \text{ kg m}^{-3}$  and  $B = 0.4 \text{ nT}$  (thus a solar wind pressure of 16 pPa ahead of the bow shock with  $V \sim 400 \text{ km/s}$ , see Figure 3b), unstable domains, hereafter called “sources,” extend over the dawn-to-noon sector ( $\leq 1100 \text{ LT}$ ) and the dusk sector ( $\geq 1800 \text{ LT}$ ) when  $V \sim 400\text{--}450 \text{ km/s}$ . These sources move toward noon when  $V$  increases, while no dusk source exists for  $V \leq 420 \text{ km/s}$ .

[10] G00 investigated the effect of solar wind fluctuations measured by Voyager 1 at Saturn on the near-noon edge of the morning source because an azimuthal displacement of the source may result in a variation of the measured radio period. They estimated (see their Figure 9) a source displacement  $\leq 15^\circ/\text{day}$ , resulting in short-term fluctuations of the radio period  $\leq 3.7\%$ . However, because the variations of  $\rho$  and  $B$ , and hence of  $\rho_1$  and  $B_1$ , are very bursty and have a large amplitude, they lead to quasi-random fluctuations of the unstable domain edges. Averaged over a  $\sim 2$ -month interval or more, these fluctuations cancel out and an unmodified radio rotation period should be measured, equal to  $P_{\text{Sat}}$ .

[11] However, we noticed in Figure 2 (as well as in Figure 9 of G00) that the solar wind velocity at Saturn varies with time in a very organized way, more regular than the other solar wind parameters: its variations follow systematically the shape of an “asymmetrical sawtooth,” with steep increases and slow decreases. This behavior results from the interaction between slow and fast solar wind streams building up interplanetary shocks during the outward propagation of the flow [Gosling *et al.*, 1976].

[12] Thus we investigate below the hypothesis that  $V$  is the dominant “control parameter” on the LT position of the SKR source and analyze the impact of its systematic variations on the radio period measured over intervals of various lengths. For that purpose, we have built two simple models. We present them below and analyze their predictions.

### 3.2. Model 1: KHI Source

[13] We first investigate the effect of a sawtooth time variation of  $V$  in the frame of an idealized KHI model whose “sources” are illustrated in Figure 3b ( $B$  and  $\rho$  are kept constant and equal to  $0.4 \text{ nT}$  and  $10^{-22} \text{ kg m}^{-3}$ , respectively). We assume that the SKR is triggered as explained above by a localized magnetic field anomaly rotating at the true sidereal period of Saturn  $P_{\text{Sat}}$ , when it crosses the sources of Figure 3 where electron precipitations are believed to be present.

[14] A model time series of SKR activity is then built as follows: the variation of  $V(t)$  is represented as a series of

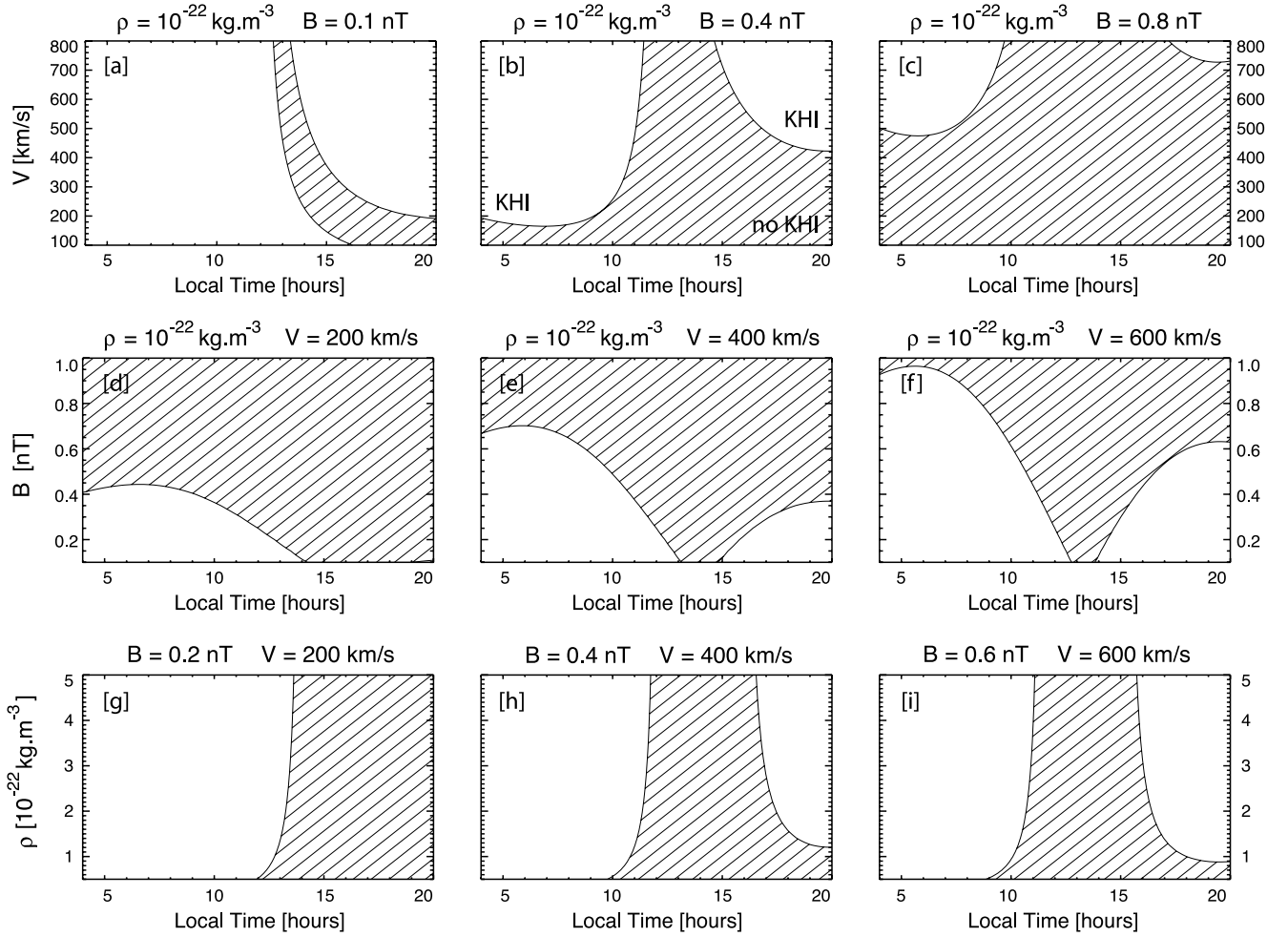


**Figure 3.** Typical KHI domains versus local time and solar wind parameters. Unstable areas ( $Q > 1$ ) are displayed in white, while stable ones are hatched. (a)–(c) Analysis of the role of the solar wind velocity  $V$ ,  $\rho$  and  $B$  being fixed for each plot. (d)–(f) Analysis of the role of  $B$ , and (g)–(i) analysis of the role of  $\rho$ . The latter appears to have little impact on the LT extent of KHI domains.

sawtooths, from  $V_{\min}$  to  $V_{\max}$ , over an interval  $T_{\text{int}}$ . Each sawtooth has a total duration  $T = T_{\text{up}} + T_{\text{down}}$  (with  $T_{\text{up}}$  the duration of the velocity increase and  $T_{\text{down}}$  that of the decrease). At each time  $t \in [0, T_{\text{int}}]$ , the value of  $V$  is thus fixed and defines (via Figure 3b) zero to two LT domains where KHI is active. Then we consider a rotating trigger, with local time:  $LT_{\text{trig}}(t) = ((t \times 24/P_{\text{Sat}}) \bmod 24)$  (hours). The SKR intensity time series is thus defined by

$$I_{\text{SKR}}(t) = \begin{cases} 1 & \text{if } Q(V(t), LT_{\text{trig}}(t)) > 1 \\ 0 & \text{if not} \end{cases} \quad (2)$$

[15] The deterministic sawtooth velocity variation and corresponding SKR intensity variations over one interval  $T$  are sketched in Figures 4a and 4b. For a more realistic representation of short- and long-term fluctuations of the modeled velocity  $V(t)$ , we also introduce a randomization parameter  $R \ll 1$ . This parameter affects as a  $(1 + rR)$  coefficient (with  $r$  a random variable with normal distribution in  $[0, 1]$ ) consecutive values of  $T_{\text{up}}$ ,  $T_{\text{down}}$  (and thus  $T$ ),  $V_{\min}$ , and  $V_{\max}$ , over the studied time interval  $T_{\text{int}}$ .  $R$  is also used as the standard deviation of modeled velocity fluctua-

tions at a timescale of a few hours. The corresponding velocity variations over an interval  $T_{\text{int}} = 90$  days are shown, with  $R = 0.2$ , in Figure 4c.

[16] We performed a parametric study of this model with  $T_{\text{int}}$  between 45 days ( $\sim 100 \times P_{\text{Sat}}$ ) and 270 days (as in the work of *Desch and Kaiser* [1981]),  $T = 26$  or 13 days (the typical period and half-period of solar wind variations at Saturn's orbit, related to the structure of corotating interaction regions),  $T_{\text{up}} = 0.1$  to 2 days,  $V_{\min} = 250$  to 350 km/s, and  $V_{\max} = 450$  to 650 km/s (the slightly extended range  $[V_{\min}, V_{\max}]$  includes possible variations of the magnetospheric subcorotation velocity  $V_2$ ), and  $R = 0$  (fully deterministic) to 0.2. For each set of parameters, we computed 100 times the Fourier spectrum of  $I_{\text{SKR}}(t)$  (with Hanning windowing) and analyzed the distributions of peak values ( $P_{\text{SKR}}$ ) of each power spectrum. The radio period was computed in this same way from observed SKR intensity time series by *Desch and Kaiser* [1981] and G00.

[17] The length of the analyzed time series  $T_{\text{int}}$  defines the resolution of the resulting power spectrum ( $1/T_{\text{int}} = 0.16\%$  to  $1\% \times P_{\text{Sat}}$ ). The  $V$  sawtooth, with a quasi-periodicity about 13 or 26 days, generates beats with  $P_{\text{Sat}}$  at  $1 \pm 1.7\%$  and  $1 \pm 3.4\% \times P_{\text{Sat}}$ . The precise value of  $T_{\text{up}}$  has no



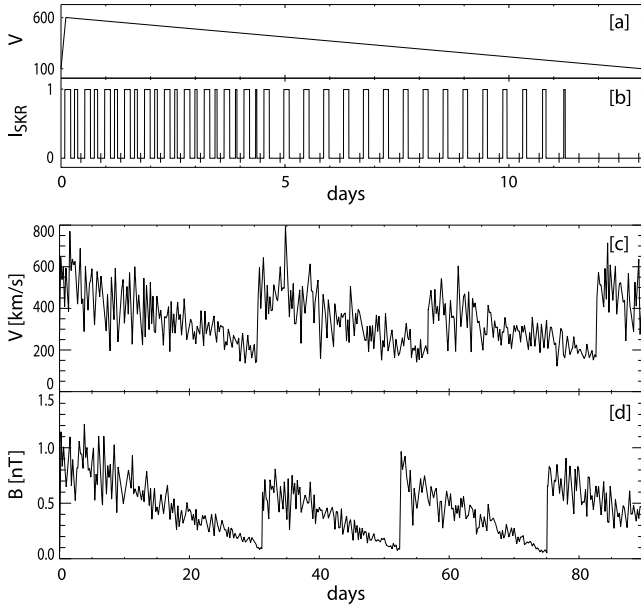


**Figure 4.** Model 1 simulation procedure: (a) Simulated sawtooth variation of the solar wind velocity  $V(t)$  over one interval  $T = 13$  days, with  $T_{up} = 0.1$  day and  $R = 0$  (fully deterministic case); (b) corresponding simulated SKR time series  $I_{SKR}(t)$ ; (c) and (d) Simulated variations of  $V(t)$  and  $B(t)$  over an interval  $T_{int} = 90$  days, with  $T = 26$  days,  $T_{up} = 0.1$  day,  $V_{min} = 250$  km/s,  $V_{max} = 550$  km/s,  $B_{min} = 0.1$  nT,  $B_{max} = 1$  nT, and  $R = 0.2$ .

influence on the result as long as  $T_{up} \ll T_{down}$ .  $V_{min}$  and  $V_{max}$  define the number of active SKR sources per rotation, as well as their LT extent. From Figure 3b we see that the source edges may move by several hours in LT when  $V$  sweeps the interval from 250 to 650 km/s, i.e., at a rate of the order of  $0.1^\circ/(\text{km/s})$ . The dusk source exists above a certain threshold ( $V > 420$  km/s in Figure 3b).

[18] With  $R = 0$ , model 1 results in a slightly broadened peak around  $P_{Sat}$ , plus secondary peaks at beats between  $T$  and  $P_{Sat}$ , reminiscent of the multiple peaks observed in Figure 1 of *Desch and Kaiser* [1981]. The latter are sometimes more intense than the peak at  $P_{Sat}$  (as illustrated in Figure 5a), so that the distribution of measured  $P_{SKR}$ , displayed in Figure 5b, reveals peaks about  $0.966 \times P_{Sat}$ ,  $0.983 \times P_{Sat}$ , and  $P_{Sat}$ .

[19] With  $R = 0.1$  to  $0.2$ , beats tend to vanish and the measured period  $P_{SKR}$  is always found in the wings of the main broad peak at  $P_{Sat}$ , generally at  $<0.3\%$  from  $P_{Sat}$ . In very few cases, the SKR spectral peaks reaches  $\sim 1\%$  below or above  $P_{Sat}$ . Figure 5c shows an example of spectral power plot for  $R = 0.2$ , and Figure 5d shows the histogram of measured peak values.

[20] We have considered up to now constant values for  $B$  and  $\rho$ , letting only  $V$  varying with time. A more realistic model should allow the interplanetary magnetic field  $B$  to vary along with  $V$ . As discussed above and illustrated in Figure 3d–3f, the LT extent of KHI domains shows large amplitude variations with  $B$  (at constant  $V$  and  $\rho$ ). We have thus modified the above model 1, replacing the constant  $B =$

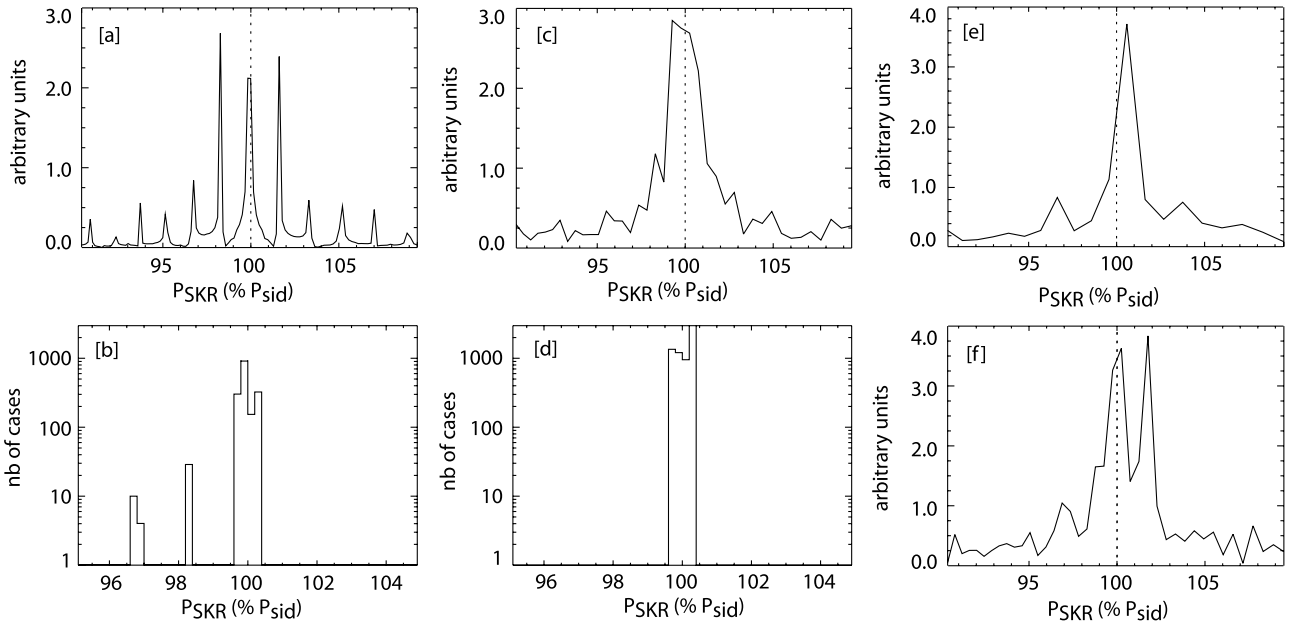


**Figure 5.** (a) Spectral power plot of  $I_{SKR}(t)$  for model 1 with parameters  $T_{int} = 270$  days,  $T = 26$  days,  $V_{min} = 250$  km/s,  $V_{max} = 650$  km/s,  $\rho = 10^{-22}$  kg m $^{-3}$ ,  $B = 0.8$  nT, and  $R = 0$ ;  $P_{SKR}$  is found at  $0.983 \times P_{Sat}$ . (b) Histogram of model 1 simulation results ( $P_{SKR}$ ) with  $R = 0$ . (c) Same as Figure 5a with  $T_{int} = 90$  days,  $T = 26$  days,  $V_{min} = 250$  km/s,  $V_{max} = 550$  km/s,  $\rho = 10^{-22}$  kg m $^{-3}$ ,  $B = 0.6$  nT, and  $R = 0.2$ ;  $P_{SKR}$  is found at  $0.993 \times P_{Sat}$ . (d) Histogram of model 1 results with  $R = 0.2$ . (e) Same as Figure 5a with  $T_{int} = 45$  days,  $T = 13$  days,  $V_{min} = 250$  km/s,  $V_{max} = 450$  km/s,  $\rho = 4 \times 10^{-22}$  kg m $^{-3}$ ,  $B_{min} = 0.1$  nT,  $B_{max} = 0.8$  nT, and  $R = 0$ ;  $P_{SKR}$  is found at  $1.002 \times P_{Sat}$ . (f) Same as Figure 5a with  $T_{int} = 90$  days,  $T = 26$  days,  $V_{min} = 250$  km/s,  $V_{max} = 550$  km/s,  $\rho = 10^{-22}$  kg m $^{-3}$ ,  $B_{min} = 0.1$  nT,  $B_{max} = 0.8$  nT, and  $R = 0.1$ ;  $P_{SKR}$  is found at  $1.018 \times P_{Sat}$ .

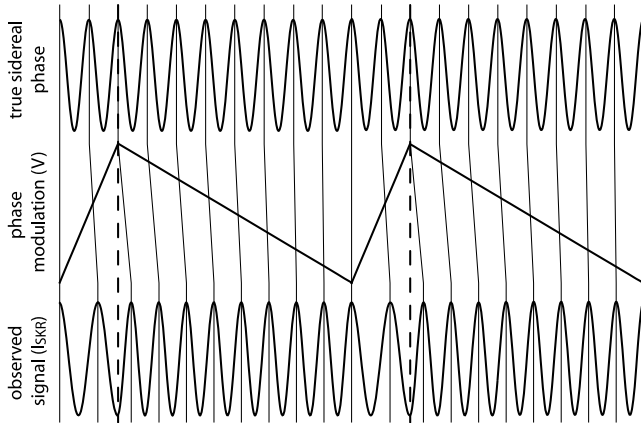


**Figure 6.** Model 2 simulation procedure: (top) a periodic (sine) function of period  $P_{\text{Sat}}$  is linearly phase-modulated by (center) an asymmetrical sawtooth. The resulting function  $I_{\text{SKR}}(t)$  is given on the bottom plot. The modulation increases the period during a short interval ( $T_{\text{up}}$ ), and then decreases it for a longer interval ( $T_{\text{down}} = T - T_{\text{up}}$ ) to get back in phase with  $P_{\text{Sat}}$ . The ratio from  $T$  to  $P_{\text{Sat}}$  is reduced in the figure (compared to the simulation) for clarity.

0.4 nT by modeled variations of  $B(t)$  between  $B_{\text{min}} \in [0.1, 0.3]$  and  $B_{\text{max}} \in [0.4, 0.8]$  nT. Long-term sawtooth variations of  $V(t)$  and  $B(t)$  are correlated, but the randomization parameter  $R$  is applied independently to the two modeled time series. This results in time series such as displayed in Figures 4c and 4d. Equation (2) thus becomes

$$I_{\text{SKR}}(t) = \begin{cases} 1 & \text{if } Q(V(t), B(t), LT_{\text{trig}}(t)) > 1 \\ 0 & \text{if not} \end{cases} \quad (3)$$

For all values of  $R$  in the range  $[0, 0.2]$ , we find results similar to those obtained above with  $R \neq 0$ , i.e., generally a single peak at a period  $P_{\text{SKR}} \in [1 \pm 0.3\%] \times P_{\text{Sat}}$  (Figure 5e). Again in very few cases, the SKR spectral peaks exceeds  $\sim 1\%$  below or above  $P_{\text{Sat}}$  (Figure 5f).

[21] We have also tested variants of the model with different SKR source definitions (morningside source only or near-noon edge of that source only) and have obtained similar results. Thus we conclude that model 1 cannot account for the 1%-level fluctuations of G00, distributed all over the range  $\sim [P_{\text{r}}, 1.01 \times P_{\text{r}}]$  between 1994 and 1997.

### 3.3. Model 2: Linear Phase-Modulated Source

[22] Idealizing and simplifying further the model for a SKR source whose LT position is controlled by the solar wind velocity, we represent now the SKR intensity time series as a periodic function of period  $P_{\text{Sat}}$ , including a time-dependent phase term linearly modulated by  $V$ . We take into account the variations of  $V$  only because (1)  $V$  plays an important role in both theories above, and (2) its variations are more systematic and regular than those of  $B$  and  $\rho$  (cf. Figure 2). With a sine as the periodic function, the simulated SKR intensity is

$$I_{\text{SKR}}(t) = I_0 \sin[2\pi(t/P_{\text{Sat}} - \alpha V(t)/360)], \quad (4)$$

where  $\alpha$  is a coupling coefficient (in  $^{\circ}/(\text{km/s})$ ).  $V(t)$  is modeled as in model 1, including the randomization parameter  $R$ , except that  $V_{\text{min}}$  and  $V_{\text{max}}$  are now given fixed values (with  $V_{\text{min}}$  arbitrarily set to 340 km/s and  $V_{\text{max}} = V_{\text{min}} + 360$  km/s) because making them variable would be redundant with variations of  $\alpha$ . Figure 6 illustrates the simulation procedure.

[23] We performed a parametric study exploring the same ranges of  $T_{\text{int}}$ ,  $T$ ,  $T_{\text{up}}$  and  $R$  as in the previous section, plus the range  $\alpha = 0.1$  to  $0.6^{\circ}/(\text{km/s})$ . The radio period was computed as above. The role of  $T_{\text{int}}$ ,  $T$ , and  $R$  is the same as above.  $T_{\text{up}}$  has again no influence in the simulation results and has been set to 0.5 day.

[24] We find for model 2 a distribution of  $P_{\text{SKR}}$  in the range  $96\% - 100\% \times P_{\text{Sat}}$ . As shown in Figure 7 (top), the parameter  $R$  is crucial in permitting the existence of  $P_{\text{SKR}}$  values not restricted to  $P_{\text{Sat}}$  and its beats with  $T$  (i.e., 1.7% and 3.4% below  $P_{\text{Sat}}$ ). Increasing  $\alpha$  (bottom of Figure 7) expands the distribution of  $P_{\text{SKR}}$  toward shorter values, as expected. Occurrences of  $P_{\text{SKR}}$  at 1% below  $P_{\text{Sat}}$  start to appear for  $\alpha \geq 0.2$ , which corresponds to an overall amplitude of the SKR source motion about  $70^{\circ}$  in LT.

[25] Only periods shorter than or equal to  $P_{\text{Sat}}$  are obtained due to our choice of  $\alpha > 0$ . This choice was made by analogy with the sense of variation of the morningside source edge versus  $V$  in the KHI source model. A different physical source model may allow for  $\alpha < 0$ , leading to symmetrical results relative to  $P_{\text{Sat}}$ . This could be for example the case if  $B$  has a dominant role in constraining the LT location of the SKR source. Note also that our results are insensitive to the shape of the  $P_{\text{Sat}}$ -periodic function: sine, truncated sine, or square functions give similar results.

[26] Figure 8 shows representative examples of the individual power spectra obtained with model 2 simulations, with  $T_{\text{up}} = 0.5$  day and  $R = 0.2$  in all cases: Figure 8a illustrates a narrow well-defined peak 1.3% below  $P_{\text{Sat}}$  obtained with parameters  $T_{\text{int}} = 90$  days,  $T = 26$  days, and  $\alpha = 0.5^{\circ}/(\text{km/s})$ . Figure 8b illustrates a result with  $P_{\text{SKR}}$  0.73% below  $P_{\text{Sat}}$ , obtained with parameters  $T_{\text{int}} = 60$  days,  $T = 26$  days, and  $\alpha = 0.4^{\circ}/(\text{km/s})$ . This result is directly comparable to the results of G00. Figures 8c and 8d were obtained with the same parameter set (two different runs with  $R = 0.2$ ,  $T_{\text{int}} = 270$  days,  $T = 26$  days, and  $\alpha = 0.6^{\circ}/(\text{km/s})$ ). They show that a narrow dominant peak  $\sim 1\%$  below  $P_{\text{Sat}}$  can be obtained over a measurement interval  $T_{\text{int}} = 270$  days provided that the coupling coefficient  $\alpha$  is larger than 0.5. A secondary peak is present at  $P_{\text{Sat}}$ . Figure 8d directly compares with the power spectrum derived from observations by *Desch and Kaiser* [1981], if we interpret their main peak as being different from  $P_{\text{Sat}}$  but  $\sim 1\%$  below it (the secondary peak at  $\sim 10$  hours 45 min being possibly the one at  $P_{\text{Sat}}$  in that case). Further simulation runs with  $T_{\text{int}} = 270$  days show that power spectra matching closely the one by *Desch and Kaiser* [1981] can be obtained with  $R = 0.2$ .

## 4. Discussion

[27] We have thus shown that it is possible to explain fluctuations of the measured radio period of Saturn ( $P_{\text{SKR}}$ ) by an asymmetrical phase modulation of the SKR source position. Model 1, directly derived from KHI unstable

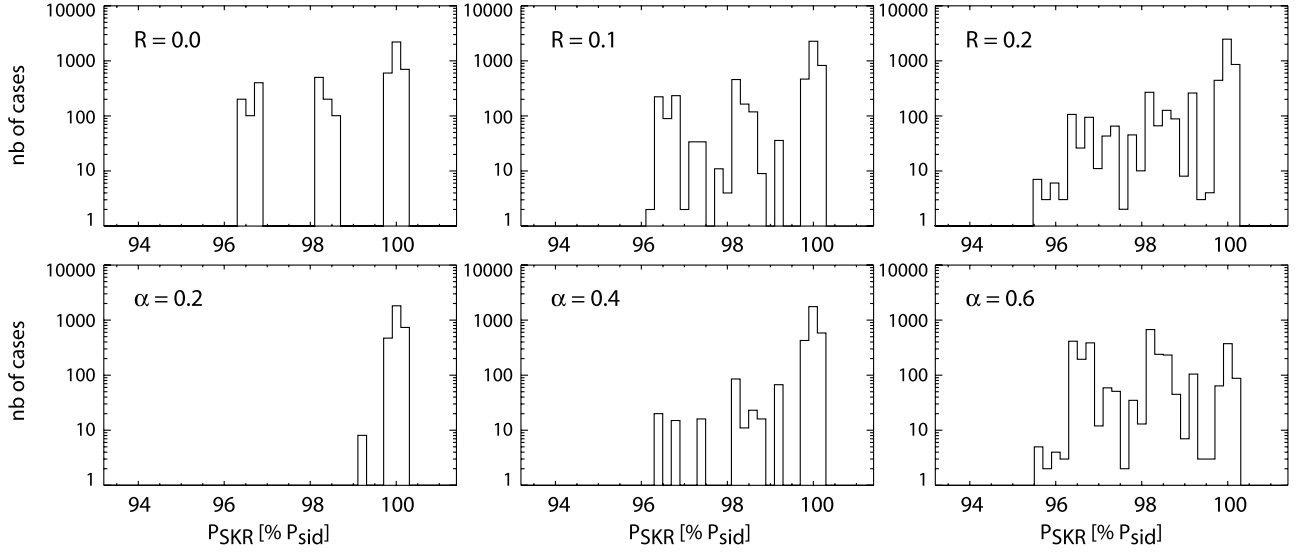


**Figure 7.** Histograms of model 2 simulation results: (top row) influence of the randomization parameter  $R$ ; (bottom row) influence of the coupling coefficient  $\alpha$  (in  $^{\circ}/(\text{km/s})$ ). One hundred eighty different parameter sets ( $T_{\text{int}}$ ,  $T$ ,  $R$ ,  $\alpha$ ) have been studied, with 100 runs performed for each.

domains modeled by G95 and G00, cannot account for fluctuations of  $P_{\text{SKR}}$  of order 1%. Model 2, where the phase of the SKR source linearly responds to solar wind fluctuations, is able to explain  $P_{\text{SKR}}$  shifted from  $P_{\text{Sat}}$  by 1 to several percent. A coupling parameter  $\alpha > 0$  implies  $P_{\text{SKR}} < P_{\text{Sat}}$ . The main peak (at  $P_{\text{SKR}}$ ) may be different from the planetary sidereal rotation period ( $P_{\text{Sat}}$ ), even for time series as long as  $T_{\text{int}} = 270$  days.

[28] This implies however  $\alpha = 0.2$  to  $0.5^{\circ}/(\text{km/s})$  (i.e., a total LT excursion of SKR sources over  $70^{\circ}$  to  $180^{\circ}$ ). The SKR source is thus probably not strictly fixed in LT but rather restricted to a limited LT sector. This could already be deduced from the initial results by *Warwick et al.* [1981]; their Figure 3 showed that SKR occurrence histograms versus subsolar longitude were identical before and after Voyager’s closest approach to Saturn, suggesting a source

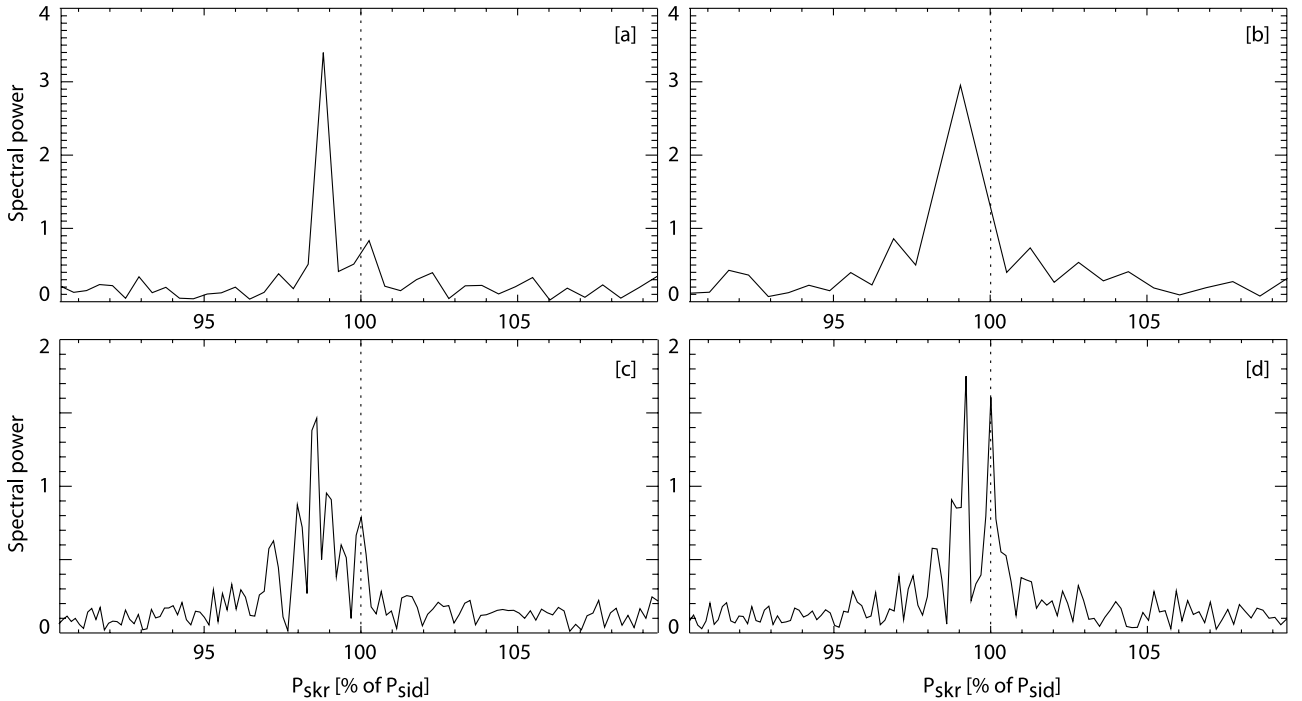


**Figure 8.** Model 2 sample spectral power plots of  $I_{\text{SKR}}(t)$  for parameters sets  $T_{\text{up}} = 0.5$  day,  $R = 0.2$ , and (a)  $T_{\text{int}} = 90$  days,  $T = 26$  days,  $\alpha = 0.5^{\circ}/(\text{km/s})$ ; (b)  $T_{\text{int}} = 60$  days,  $T = 26$  days,  $\alpha = 0.4^{\circ}/(\text{km/s})$ ; (c) and (d)  $T_{\text{int}} = 270$  days,  $T = 26$  days,  $\alpha = 0.6^{\circ}/(\text{km/s})$ . The measured  $P_{\text{SKR}}$  values are 0.988 (Figure 8a), 0.993 (Figure 8b), 0.986 (Figure 8c), and 0.993  $P_{\text{Sat}}$  (Figure 8d).

fixed in LT instead of rotating with the planet; however, the maximum of these histograms was  $>100^\circ$  broad so that the instantaneous SKR source may well move within it. Later works confirmed the statistically broad extent of SKR sources: Zarka [1988] found a good correlation between SKR intensity fluctuations seen by Voyager 1 and 2, then separated by  $\sim 135^\circ$ , on timescales greater than a half hour. G95 and previous authors also found SKR sources statistically extended in LT. More recently, Kurth *et al.* [2005] and Clarke *et al.* [2005] found a partial corotation of UV aurora related to SKR. In addition, the large value of  $\alpha$  may be understood through the three-dimensional geometry of the SKR beaming: the emission diagram being nonisotropic (probably a hollow cone [cf. Kurth *et al.*, 2005, and references therein]), small variations of the true source longitude, via related latitudinal variations of the SKR beam orientation, may lead to large apparent motions of the source as characterized by  $\alpha$ . As a comparison, the  $\pm 3.3^\circ$  variation of the Earth's declination as seen from Jupiter leads to large apparent intensity variations and radiosome motions [Alexander *et al.*, 1979; Barrow, 1981].

[29] Our results suggest that the velocity shear between magnetospheric subcorotating plasma and magnetosheath flowing plasma plays a major role in the process leading to electron precipitation.  $V(t)$ , as a nonrandomly variable “control parameter”, has thus a strong influence on the LT position of the SKR source(s). Both models, if fed with a symmetrical sawtooth or random variations of  $V$ , lead to  $P_{\text{SKR}} = P_{\text{Sat}}$ . If our above results are confirmed by further studies, they would imply that either the KHI source model requires deep modifications, or that another SKR generation model is to be preferred, as for instance the “FAC” model by Cowley *et al.* [2004]. The results from model 2 are not tied to a specific physical model of Saturn's radio (and UV) auroras. For example, if a purely latitudinal variation of the SKR source, combined to anisotropic SKR beaming, leads, for a fixed observer, to an apparent source motion in LT, this would still be consistent with our proposed explanation for the variable radio period observed provided that  $V$  controls the latitudinal variation of the source.

[30] In the frame of our model 2 assumptions and results, observations from Voyager, Ulysses, and Cassini considered together suggest that  $P_{\text{Sat}}$  is  $\sim 1\%$  larger than  $P_{\text{I}}$ , i.e.,  $P_{\text{Sat}} \sim 10$  hours 45 min. A secondary peak at this value is present in Voyager SKR data. The different values of  $P_{\text{SKR}}$  found at different epochs would thus be only related to the different structure of corotating interaction regions in the solar wind at the time of the measurements. This different structure need not be large scale and prominent in solar wind data, as we have seen above (Figures 8c and 8d) that simulations based on the same parameter set differing only by the 20% fluctuations introduced by the parameter  $R$  may lead to values of  $P_{\text{SKR}}$  over the whole range  $96\% - 100\% \times P_{\text{Sat}}$ . Note that a sidereal rotation period  $P_{\text{Sat}} \sim 10$  hours 45 min, when compared to the periods deduced from cloud tracking versus latitude ([Sanchez-Lavega *et al.*, 2000]), implies that the whole atmosphere of Saturn is in superrotation with eastward jets faster than 500 m/s.

[31] Further studies will include tests of the above models by comparing  $P_{\text{SKR}}$ , measured with Voyager, Ulysses, and Cassini radio data over intervals of various lengths ( $T_{\text{int}}$ ), with model predictions based on  $V(t)$  profiles measured

simultaneously by the same or other spacecraft and projected to Saturn. Direction-finding capabilities available on Cassini [Cecconi and Zarka, 2005] should help solve this question by making instantaneous “images” of SKR sources.

[32] Finally, we mentioned in the introduction a relative accuracy  $\sim 10^{-6}$  on Jupiter's sidereal period derived from 24-year radio data sets. Io-induced emissions dominate the Jovian decameter spectrum, and the longitude of their source depends on the Alfvén travel time  $t_A$  from Io to Jupiter, leading to an angle  $\theta_A = 2\pi t_A / P_{\text{Jup}}$  (with  $P_{\text{Jup}} = 9$  hours 55.5 min) between Io's instantaneous field line and the radiosome field line [Queinnec and Zarka, 1998]. Galileo's measurements in 1995–1997 suggest an Io plasma torus twice as dense as during Voyager flybys in 1979 [Bagenal *et al.*, 1997], implying an increase of  $\theta_A$  by  $10^\circ$  to  $20^\circ$ . This would imply a relative error on  $P_{\text{Jup}}$  of the order of  $(\theta_A/360^\circ) \times (P_{\text{Jup}}/24 \text{ years}) \sim 1 - 2 \times 10^{-6}$ , equal to the above accuracy.

[33] Accuracy in planetary rotation period determination appears thus directly related to time variations of the parameter(s) controlling the planet's radio emissions. Runs of our model 2 with  $T_{\text{int}} = 500$  to 1000 days suggest that determining Saturn's sidereal period with an accuracy  $\ll 1\%$  will require SKR time series of the order of 1.5 to 3 years that will be analyzed as a whole and by overlapping slices of 6–12 months (a peak at  $P_{\text{Sat}}$ , even if not dominant, appears in most spectral power plot with  $T_{\text{int}} > 180$  days, see e.g., Figures 8c and 8d). An independent measurement of  $P_{\text{Sat}}$  could also be obtained through the analysis of long-term variations within time series of in situ measurements of Saturn's magnetic field by Cassini.

[34] **Acknowledgment.** Arthur Richmond thanks Emma Bunce and Patrick Galopeau for their assistance in evaluating this paper.

## References

- Alexander, J. K., M. D. Desch, M. L. Kaiser, and J. R. Thieman (1979), Latitudinal beaming of Jupiter's low frequency radio emissions, *J. Geophys. Res.*, **84**, 5167–5174.
- Bagenal, F., F. J. Cray, A. I. F. Stewart, N. M. Schneider, D. A. Gurnett, W. S. Kurth, L. A. Frank, and W. R. Paterson (1997), Galileo measurements of plasma density in the Io torus, *Geophys. Res. Lett.*, **24**, 2119–2122.
- Barrow, C. H. (1981), Latitudinal beaming and local time effects in the decametre-wave radiation from Jupiter observed at the earth and from Voyager, *Astron. Astrophys.*, **101**, 142–149.
- Cecconi, B., and P. Zarka (2005), Direction finding and antenna calibration through analytical inversion of radio measurements performed using a system of two or three electric dipole antennas on a three-axis stabilized spacecraft, *Radio Sci.*, **40**, RS3003, doi:10.1029/2004RS003070.
- Clarke, J. T., et al. (2005), Morphological differences between Saturn's ultraviolet aurorae and those of Earth and Jupiter, *Nature*, **433**, 717–719.
- Cowley, S. W. H., E. J. Bunce, and R. Prangé (2004), Saturn's polar ionospheric flows and their relation to the main auroral oval, *Ann. Geophys.*, **22**, 1379–1394.
- Desch, M. D. (1982), Evidence for solar wind control of Saturn radio emission, *J. Geophys. Res.*, **87**, 4549–4554.
- Desch, M. D., and M. L. Kaiser (1981), Voyager measurement of the rotation period of Saturn's magnetic field, *Geophys. Res. Lett.*, **8**, 253–256.
- Desch, M. D., and H. O. Rucker (1983), The relationship between Saturn kilometric radiation and the solar wind, *J. Geophys. Res.*, **88**, 8999–9006.
- Galopeau, P., and A. Lecacheux (2000), Variations of Saturn's radio rotation period measured at kilometer wavelengths, *J. Geophys. Res.*, **105**, 13,089–13,102.
- Galopeau, P., and P. Zarka (1992), Reply to comment on “Evidence of Saturn's magnetic field anomaly from Saturnian kilometric radiation high-frequency limit,” *J. Geophys. Res.*, **97**, 12,291–12,297.
- Galopeau, P., P. Zarka, and A. Ortega-Molina (1991), Evidence of Saturn's magnetic field anomaly from Saturnian kilometric radiation high-frequency limit, *J. Geophys. Res.*, **96**, 14,129–14,140.



- Galopeau, P., P. Zarka, and D. Le Quéau (1995), Source location of Saturn's kilometric radiation: The Kelvin-Helmholtz instability hypothesis, *J. Geophys. Res.*, **100**, 26,397–26,410.
- Gosling, J. T., A. J. Hundhausen, and S. J. Bame (1976), Solar wind stream evolution at large heliocentric distances: Experimental demonstration and the test of a model, *J. Geophys. Res.*, **81**, 2111–2122.
- Gurnett, D. A., W. S. Kurth, and F. L. Scarf (1981), Plasma waves near Saturn: Initial results from Voyager 1, *Science*, **212**, 235–239.
- Gurnett, D. A., et al. (2005), Radio and plasma wave observations at Saturn from Cassini's approach and first orbit, *Science*, **307**, 1255–1259.
- Higgins, C. A., T. D. Carr, F. Reyes, W. B. Greenman, and G. R. Lebo (1997), A redefinition of Jupiter's rotation period, *J. Geophys. Res.*, **102**, 22,033–22,041.
- Kaiser, M. L., M. D. Desch, J. W. Warwick, and J. B. Pearce (1980), Voyager detection of nonthermal radio emission from Saturn, *Science*, **209**, 1238–1240.
- Kurth, W. S., and P. Zarka (2001), Saturn radio waves, in *Planetary Radio Emissions*, vol. V, edited by H. O. Rucker, M. L. Kaiser, and Y. Leblanc, p. 247, Austrian Acad. of Sci. Press, Vienna.
- Kurth, W. S., et al. (2005), An Earth-like correspondence between Saturn's auroral features and radio emission, *Nature*, **433**, 722–725.
- Ladreiter, H. P., P. Galopeau, and P. Zarka (1994), The magnetic field anomaly of Saturn, paper presented at International Symposium on Magnetospheres of Outer Planets, Aust. Acad. of Sci., Graz, Austria.
- Prangé, R., L. Pallier, K. C. Hansen, R. Howard, A. Vourlidas, R. Courtin, and C. Parkinson (2004), An interplanetary shock traced by planetary auroral storms from the Sun to Saturn, *Nature*, **432**, 78–81.
- Queinnec, J., and P. Zarka (1998), Io-controlled decameter arcs and Io-Jupiter interaction, *J. Geophys. Res.*, **103**, 26,649–26,666.
- Sanchez-Lavega, A., J. F. Rojas, and P. V. Sada (2000), Saturn's Zonal Winds at Cloud Level, *Icarus*, **147**, 405–420.
- Thompson, W. B. (1983), Parallel electric fields and shear instabilities, *J. Geophys. Res.*, **88**, 4805–4812.
- Trauger, J. T., et al. (1998), Saturn's hydrogen aurora: Wide field and planetary camera 2 imaging from the Hubble Space Telescope, *J. Geophys. Res.*, **103**, 20,237–20,244.
- Warwick, J. W., et al. (1981), Planetary radio astronomy observations from Voyager 1 near Saturn, *Science*, **212**, 239–243.
- Zarka, P. (1988), Beaming of planetary radio emissions, in *Planetary Radio Emissions II*, pp. 327–342, Aust. Acad. of Sci. Press, Vienna.
- Zarka, P., and W. S. Kurth (2005), Radio wave emission from the outer planets before Cassini, *Space Sci. Rev.*, **116**, 371–397.

---

B. Cecconi, Department of Physics and Astronomy, University of Iowa, 203 Van Allen Hall, Iowa City, IA 52242, USA. (baptiste-cecconi@uiowa.edu)

P. Zarka, Laboratoire d'Etudes Spatiales et d'Instrumentation en Astrophysique, Centre National de la Recherche Scientifique, Observatoire de Paris, 5 place Jules Janssen, F-92195 Meudon, France.